PCCP

PAPER

View Article Online
View Journal | View Issue

Cite this: *Phys. Chem. Chem. Phys.*, 2019, **21**, 8729

Multitribe evolutionary search for stable Cu–Pd–Ag nanoparticles using neural network models†

Samad Hajinazar, Ernesto D. Sandoval, Aiden J. Cullo and Aleksey N. Kolmogorov

Received 11th February 2019,
Accepted 2nd April 2019

DOI: 10.1039/c9cp00837c

rsc.li/pccp

We present an approach based on two bio-inspired algorithms to accelerate the identification of nanoparticle ground states. We show that a symbiotic co-evolution of nanoclusters across a range of sizes improves the search efficiency considerably, while a neural network constructed with a recently introduced stratified training scheme delivers an accurate description of interactions in multielement systems. The method's performance has been examined in extensive searches for stable elemental (30–80 atoms), binary (50, 55, and 80 atoms), and ternary (50, 55, and 80 atoms) Cu–Pd–Ag clusters. The best candidate structures identified with the neural network model have consistently lower energy at the density functional theory level compared with those found with traditional interatomic potentials.

1 Introduction

Materials downsized to the nanoscale display surface-defined functionalities desirable in catalysis,[1] solar energy conversion,[2] medicine,[3] *etc.* Compared to their bulk counterparts, nanoparticles (NP) have a wider range of properties because they are not constrained by the translational symmetry and can be synthesized in various size-dependent metastable structures. The dramatic expansion of the configuration space complicates the identification of chemical compositions and synthesis conditions optimal for NPs' targeted applications. Despite the recent development of advanced modeling methods, the basic problem of determining stable structures as a function of the system size and constituent elements remains a considerable challenge.[4–6]

The success of predicting stable structures depends on the efficiency of the search algorithm and the quality of the interatomic interaction description. It has been widely acknowledged that no single search method can provide the best convergence for all cases.[5–20] As a result, existing optimization algorithms span a wide spectrum of strategies that rely on unbiased sampling (*e.g.*, in *ab initio* random structure searching[21]), take advantage of common motifs (*e.g.*, in dynamic lattice searching[16–18,22]), or balance unconstrained optimization with explicit or implicit biases (*e.g.*, evolutionary algorithm, basin hopping method, particle swarm optimization, *etc.*[8–11]). Similarly, the toolset of interaction description methods offers a range of options with varying degrees of accuracy and efficiency. Density functional theory (DFT) has been used to model properties of select NPs up to a few thousand atoms,[23,24] but the method's N^3 scaling restricts fully *ab initio* structure searches to systems with typically a few dozen atoms.[25,26] The use of linearly scaling classical potentials extends the unconstrained search range to hundreds of atoms, but the models' limited transferability poses a problem for resolving competing structures.[6] Hybrid strategies mitigating this issue have relied on complementary DFT calculations for either adjusting classical potentials during structure searches[27] or assessing small pools of global minima candidate structures.[28] The recent introduction of neural network (NN) interatomic models has made it possible to maintain near *ab initio* accuracy of the total energy description across different atomic environments.[29–37]

Machine learning-based atomistic force fields have already been used for predicting crystalline or nanosized materials. Examples of bulk systems include high-P or high-T crystalline phases of Si,[38] B,[39] and Mg–Ca,[40] while stable surface configurations have been explored for the Cu–ZnO[41] and Au–Pd[42] systems. The most extensive effort has been directed at the identification of stable clusters. NN potentials have been developed to perform unconstrained ground state searches for elemental Na_n clusters (n = 17–40),[43] MgO-supported Pt_{13},[44] Au_{58},[45] $Au_{17,34,58}$,[46] and Au_{147}.[47] Select compositions and sizes have been examined in multielement systems as well, such as 55-atom Cu–Au clusters in water solution,[48] 55-atom Ag–Au structures,[49] and Pt–Cu–Ni clusters with 147, 309, and 561 atoms.[50] Surprisingly we did not find any comprehensive work dedicated to benchmarking NN against traditional potentials in global structure searches.

Department of Physics, Applied Physics and Astronomy, Binghamton University, State University of New York, PO Box 6000, Binghamton, New York 13902-6000, USA

† Electronic supplementary information (ESI) available. See DOI: 10.1039/c9cp00837c

In this study, we have performed a systematic comparison of the potential energy surface (PES) mapping at zero temperature provided by the widely used Gupta potentials and our NN potentials developed for the Cu–Pd–Ag system. NPs comprised of these precious/noble metals have applications in energy conversion and storage, medicine, optics, electronics, *etc.*[51] In the elemental NP form, Cu enhances the activity of composite catalysts in numerous electro- and photocatalytic reactions by promoting the formation of C–C bonds and facilitating the separation of electron–hole pairs,[52,53] Ag exhibits a high antimicrobial activity suitable for use in medicine,[54] and Pd displays good catalytic properties for a range of (electro)chemical reactions.[55] In the nanoalloy form, Cu–Ag NPs have a high density of states at the Fermi level and are considered promising alternatives to expensive Pt-based catalysts,[56] while Cu–Pd NPs in nanodendrite structures have high specific and mass activities important for the electrocatalytic methanol oxidation reaction.[57] Cu–Pd–Ag NPs have been the subject of numerous structure analysis studies.[7] Several DFT studies have focused on small elemental Cu, Ag, and Pd clusters,[25,58–60] which included evolutionary optimization of the three metals in the 12–25 atom range.[26] Binary Cu–Ag and Pd–Ag clusters of magic 34, 38, and 55 sizes have been examined with a Gupta potential-assisted DFT search driven by the basin hopping method.[61–67] Embedded atom model studies have included explorations of large-size systems with up to a few hundred atoms.[68–70] Studies based on Sutton–Chen potential have been performed for Cu and Ag[71,72] as well as Cu–Ag,[73] with a notable lack of parameterizations available for Pd and the corresponding binaries. The most recent and extensive studies have been done with the Gupta potential,[22,74–77] which motivated us to test our NNs against this widely used classical model.

Recent extensive ground state searches based on the Gupta potentials yielded libraries of low-energy structures for elemental Cu, Pd, and Ag[22] as well as binary Cu–Ag and Pd–Ag[61,63–67,78] clusters. The availability of these reference sets helped us test the performance of the machine learning-based approach and establish the NN's consistently better description of the elemental and binary systems. Namely, 62.7% of the lowest-energy elemental structures identified in our NN-based searches turned out to be more stable (with 26.1% by over 10 meV per atom) compared with the Gupta reference structures after both sets were locally optimized with DFT. An additional advantage of the NNs over simple classical potentials is the treatment of 3-body terms that enables accurate description of ternary alloys. We used our model to identify Cu–Pd–Ag stability regions for select sizes and observed a good prediction quality with follow-up DFT calculations.

The use of NNs instead of traditional potentials generally increases the computational cost of simulations by two-three orders of magnitude.[79–82] With the primary goal of examining the models' performance for a variety of nanosized configurations, we have introduced and tested an improved evolutionary algorithm that executes a concurrent optimization of clusters in a specified size range. The search acceleration is achieved by periodic exchange of the most stable members among tribes of neighboring NP sizes. We have also introduced and examined the performance of different evolutionary operations that include a Tetris-based generation of NPs, an alternative core–shell crossover, and a Rubik's cube mutation.

2 Interaction description methods

2.1 Density functional theory calculations

DFT served as the reference electronic structure method for evaluating total energies and atomic forces. By default, we used the Perdew–Burke–Ernzerhof (PBE) exchange–correlation functional[83] within the generalized gradient approximation (GGA),[84] and projector augmented wave potentials (Cu_pv, Pd_pv, and Ag)[85] implemented in VASP.[86,87] All calculations were performed with a high 500 eV energy cutoff and without spin polarization or spin–orbit coupling. Generation of reference bulk structures for NN training was done with dense ($\Delta k \sim 0.04$ Å^{-1}) k-point meshes[62] and the Methfessel–Paxton[88] 0.1 eV smearing. The settings typically provide a 2–3 meV per atom numerical convergence for relative energies of different structures. We kept the same smearing method in Γ-point simulations of NPs placed in 20 Å cubic unit cells. Our tests indicated that the NP relative energies varied by less than 0.5 meV per atom upon reduction of the smearing parameter or expansion of the box size. Although improvements in describing the energetics are observed with revised versions of the PBE functional,[89] the original PBE form has been widely used for the generation of NN training datasets.[36,40,90–93] Since we had used the PBE parametrization for the construction of NN potentials in our previous study,[36] we expanded the reference set in this work with the same DFT flavor, referred to as the GGA hereafter. Select structure sets were also evaluated with the local density functional approximation (LDA)[94] (Section 4) and with the RPBE functional to assess the DFT systematic errors (Table S1, ESI†).

2.2 Gupta potential

The Gupta potential (GP) was introduced to treat many-body effects within a second-moment approximation of the tight-binding method[95,96] and has been widely used for modeling metallic alloys.[74–77] The potential has the following functional form:

$$\sum_{j\neq i}^{N} A_{ij} \mathrm{e}^{-p_{ij}\left(r_{ij}/r_{ij}^{(0)}-1\right)} - \left\{\sum_{j\neq i}^{N} \zeta_{ij}{}^{2} \mathrm{e}^{-q_{ij}\left(r_{ij}\Big/r_{ij}^{(0)}-1\right)}\right\}^{1/2},$$

where A_{ij}, ζ_{ij}, p_{ij}, q_{ij}, and $r_{ij}^{(0)}$ are adjustable parameters.

The cohesive term is a function of only pair interactions; therefore, it cannot be properly tuned to describe ternary alloys. Table 1 lists GP parameters used for the elemental and binary systems considered in the present study. All these parameterizations were based on experimental data: lattice constants, elastic constants, cohesive energy for elemental systems, and solubility enthalpies for the binary compounds.

Table 1 GP parameters used in this study. The elemental parameters for Ag are from ref. 76, and Cu and Pd parameters are from ref. 75. The binary parameters for Cu–Ag and Pd–Ag NPs are from ref. 74

Model	A_{ij} (eV)	ξ_{ij} (eV)	p_{ij}	q_{ij}	$r_{ij}^{(0)}$ (Å)
Cu	0.0855	1.2240	10.96	2.278	2.556
Pd	0.1746	1.7180	10.867	3.742	2.7485
Ag	0.1043	1.194	10.79	3.19	2.88
Cu	0.0894	1.2799	10.55	2.43	2.556
Ag	0.1031	1.1895	10.85	3.18	2.8921
Cu–Ag	0.0980	1.2274	10.70	2.805	2.72405
Pd	0.175	1.7019	11.0	3.794	2.75
Ag	0.1031	1.1899	10.85	3.18	2.89
Pd–Ag	0.1607	1.5597	10.895	3.492	2.82

2.3 Neural network parametrization

Known shortcomings of semiempirical potentials[27,97,98] have motivated the development of more adaptable interatomic models.[27] NNs are among the most general and flexible machine learning methods that have been gaining prominence in materials modeling since the introduction of descriptors capable of converting arbitrary atomic environments into NNs' input.[29,99] It has been shown that NNs trained on large first-principles datasets outperform traditional potentials in the description of total energies, defect energies, phonon dispersions, transition states, *etc.* for elemental or multicomponent systems.[100,101]

Construction of NN models for the present analysis of Cu–Pd–Ag NPs was based on the approach introduced in our previous study.[36] A reliable sampling of the relevant PES regions is achieved *via* short evolutionary searches rather than commonly used molecular dynamics runs. The former protocol promotes the inclusion of diverse non-equilibrium configurations occurring in global structure searches and limits the undesired function of the NN as an extrapolator. A consistent description of interactions in alloys is attained *via* a hierarchical training from the bottom up, *i.e.*, starting from elements and proceeding to binaries and ternaries. The training stratification ensures that the NN expansion to chemical systems with more elements does not affect the description of the subsystems, as only the new interspecies weights are allowed to adjust. The benefits of these data generation and NN training schemes were examined in systematic tests for bulk Cu–Pd–Ag structures.[36]

In order to account for the more diverse atomic environments in NPs we have made the following adjustments in the NN parameterization. First, we incorporated GGA atomic forces into the training set, which provides local information about interatomic interactions.[79–82,102] Since forces on nearby atoms are correlated, it was found sufficient to select 25% of atoms randomly and treat each of the three force components per atom as a reference data point (see Table S2, ESI†).[102] Second, we used the L_2 regularization with $L = 10^{-6}$ to promote the smoothness of the PES fit. We observed that the regularization had little effect on the NN performance because we maintained a reasonably high (at least 18 : 1) data to parameter ratio in all considered cases. Third, we expanded the set of Behler–Parrinello symmetry functions from 30 to 51 per element and increased the cutoff radius from 6.0 Å to 7.5 Å with the corresponding reduction of all η parameters by a factor of 1.25^2 (Table S3, ESI†).[40] Our tests showed that the diverse low-coordination surface geometries were described better with the 51-function basis set than with the 30-function set used for studying the bulk materials,[36] which is important for resolving competing NP configurations. The larger cutoff helps capture long-range effects and enables future use of these Cu, Pd, and Ag NN models in combination with larger elements. Last, we complemented the previously described database of crystalline structures[36] with NP configurations. The reference NP structures were generated with short evolutionary searches using the previously developed bulk NN model.[36] The resulting dataset consisted of (i) non-equilibrium bulk structures with 1–12 atoms per unit cell (∼85%); (ii) compressed/expanded close-packed structures and small clusters to reduce the number of artificial minima appearing in unconstrained searches as discussed in ref. 36 (∼10%); and (iii) clusters with 30–80 atoms for single elements and 55 atoms for alloys (∼5%). All constructed NNs had two hidden layers with 10 neurons each, and the total number of adjustable weights is given in Table 2. We split the data randomly into training and testing sets with a typical 90% to 10% ratio. The only subset used exclusively for training was the collection of compressed/expanded structures described in (ii) above. Because of this choice, the training errors were about 7.5% larger than the testing errors, as detailed in Table 2 and Fig. S1 (ESI†).

2.4 Method comparison

The following tests illustrate the performance of the NN model relative to the GGA, the LDA, the GP, and our previous NN^{bulk} model trained on only bulk structures.[36] According to Tables 2 and 3, the inclusion of the NP reference data tunes the NN to describe both bulk and cluster configurations with a good 3–10 meV per atom accuracy. The NN^{bulk} model extrapolates the surface energies of close-packed structures well (Fig. S2, ESI†) but evaluates the total energies of NPs with large average errors of 50–70 meV per atom (Fig. S3, ESI†). As can be seen from the mean values of the error distributions in Table 3, the lack of low-coordinated atomic configurations in the NN^{bulk} training set resulted in the model's consistent overestimation of the NP cohesive energies.

Table 2 The NN parameterization specifications broken down by the chemical composition: the total number of adjustable weights, the number of energy and force components in the training sets, and the NN testing RMSEs for energies (meV per atom) and forces (eV Å^{-1}). The GGA was used as a reference method for the NN training and testing

Model	# of weights	# of E data	# of F data	Error E	Error F
Cu	641	2916	19 581	4.3	0.043
Pd	641	2844	19 683	8.6	0.073
Ag	641	2907	19 635	3.6	0.042
Cu–Pd	1880	3725	32 223	6.6	0.063
Cu–Ag	1880	3724	32 034	3.5	0.038
Pd–Ag	1880	3705	32 166	4.8	0.058
Cu–Pd–Ag	1290	2191	29 163	5.2	0.053

Table 3 RMSEs of NN models in evaluating the total energies (in meV per atom) of bulk and NP datasets, with respect to GGA values. The NN^{bulk} and NN are models trained using bulk only and bulk plus NP datasets, respectively. The second row of numbers for each dataset reflects the mean value of error distribution for the corresponding model (see Fig. S3, ESI)

		Cu		Pd		Ag	
Dataset		NN^{bulk}	NN	NN^{bulk}	NN	NN^{bulk}	NN
Bulk	RMSE	4.6	4.0	10.6	8.7	4.6	3.3
	Mean	−0.1	0.0	−0.9	0.1	0.0	0.0
NP	RMSE	69.5	15.3	70.1	12.3	50.1	12.6
	Mean	−60.2	0.4	−64.3	−2.3	−21.1	−0.9

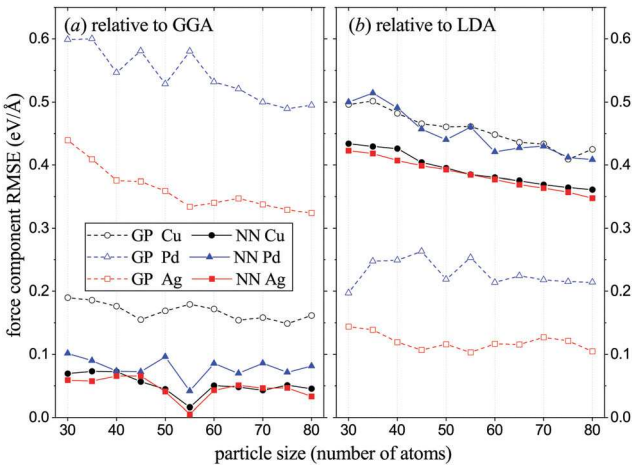

Fig. 1 Accuracy of atomic force description with the NN and GP models relative to the two DFT approximations. The RMSEs were evaluated for the lowest-energy Cu, Pd, and Ag structures found with the corresponding NN or GP interaction model.

Fig. 1 details how the NN and the GP describe atomic forces relative to the two DFT approximations. The considered NN and GP structures were putative ground states found with the respective classical model for the elemental systems (Section 4). Since the structures were fully relaxed at the NN or the GP level, the root-mean-square error (RMSE) of forces evaluated with the DFT approximations provides useful information on how close the configurations are to being local minima on the DFT PES. Against the GGA, we observed a good agreement for the NN (with the errors below 0.1 eV $Å^{-1}$ for all three metals) and a large discrepancy for the GP (with the errors in the 0.3–0.6 eV $Å^{-1}$ range for Pd and Ag). Against the LDA, the force error values for the NN and the GP effectively flipped. The results suggest that the empirical GP might be providing reasonable NP geometries, as the GGA and LDA are known to overestimate and underestimate bond lengths, respectively. However, our results in Section 4 illustrate that the GP local minima configurations turn out to be consistently less stable than the NN configurations once both sets are relaxed with either the LDA or GGA method.

In a final set of benchmark tests, we examined the PES profiles for non-equilibrium configurations obtained by rotating one atom about a NP (see Fig. S4 and S5, ESI†). The atom's radial distance was optimized for a series of angles at the GGA level and the resulting structures were evaluated with the four methods. Interestingly, the LDA proved to be the odd one out, differing from the other methods by up to 100% in the description of the relative energies along this partially constrained transition state path. The NN and GP showed a good agreement with the GGA, describing the energy barriers to within ∼20%. The main purpose of the test was to check whether the flexible NN models would develop clearly artificial minima corresponding to low-coordination surface configurations. The results for the considered elemental and binary NPs demonstrated a reasonably good performance of the developed NN models.

3 Structure search algorithm

3.1 Overview of optimization methods

A number of advanced optimization techniques have been adapted for finding NP ground states. Basin-hopping represents an efficient procedure for escaping from local minima and mapping the PES;[12–14] particle swarm optimization relies on the crowd intelligence for navigating the energy landscape;[19,20] evolutionary algorithm mixes and propagates beneficial structural traits;[103–105] and dynamic lattice searching takes advantage of known structural motifs.[16–18,22]

While these algorithms differ in implementation and performance for different PES topologies, there are a few guiding principles that the successful approaches have in common. The search efficiency is generally improved by avoiding the consideration of similar candidate structures, which is achieved by creating taboo lists of visited local minima or eliminating duplicate members in the population. It is also beneficial to incorporate relevant information or optional constraints into unbiased searches in the form of known structure seeds or symmetrization operations. Even with these features present, optimization algorithms typically screen 10^3–10^4 structures to identify ground states for clusters with 50–100 atoms.[12] Therefore, the computational cost could be a factor limiting the scope of stability analysis when the atomic interactions are modeled with NNs rather than semiempirical potentials.

The evolutionary algorithm implemented in MAISE[106] has been extensively used for bulk[40,107–110] and film[111] materials leading to confirmed predictions of some of the largest new structures with 10 (FeB_4,[107] CrB_4[112]), 20 (MnB_4[109]), 28 (CaB_6[108]), and 56 ($Na_3Ir_3O_8$[110]) atoms per primitive unit cell. In this work, we extended the application range to NPs by implementing and improving the evolutionary-driven optimization for non-periodic configurations. We benchmarked the method using the less expensive GP against the low-energy structures found previously with dynamic lattice searching for elemental Cu, Pd, and Ag clusters with 30–80 atoms.[22]

3.2 Evolutionary operations

Population initialization is one of the critical steps in the PES sampling. Use of common structural motifs may speed up the identification of ground states by order(s) of magnitude,[108] but

may also steer the search away from unexpected or unknown morphologies. We chose not to rely on any prior information except for the effective atomic sizes and generate structures randomly, ensuring the absence of unphysically short interatomic distances. The creation of meaningful starting geometries is especially important in NN calculations because the inclusion of high-energy configurations reduces the NN accuracy in the relevant low-energy PES regions. In the case of periodic structures, we avoided short distances in randomly generated unit cells by allowing 5–10 gradient descent steps with a purely repulsive pair potential. In the case of NPs, we kept atoms contained by adding a parabolic energy penalty for atomic positions beyond a spherical boundary at the cluster's estimated radius. We also implemented an alternative generation scheme inspired by the game of Tetris. Atoms are shot from random directions towards the NP one by one and repeatedly rotated to explore allowed positions closer to the cluster's center (Fig. 2(a)). The algorithm was particularly helpful for generating nanoalloys with desired radius- or angle-dependent species distributions. Both schemes proved to be efficient for creating random compact NPs up to at least a few hundred atoms. In fact, the good packing achieved in these approaches led to an apparent bias towards spherical configurations. We promoted the generation of ellipsoidal shapes by introducing a diagonal covariance matrix $\Lambda = \mathrm{diag}(\varepsilon^{-1/2}, \varepsilon^{-1/2}, \varepsilon)$ in the calculation of the atomic distances to the origin $d_i^2 = r_i \Lambda r_i$. A single ellipticity parameter ε was randomly chosen in the 0.7–1.3 range, and the principal axis was randomly oriented along x, y, or z.

The central feature of evolutionary optimization is the crossover operation that creates offspring by combining pieces of two parent structures. The partitioning is commonly done in the form of planar cuts through each parent that select parts of roughly equal size (Fig. 2(c)). As has been observed and discussed in previous studies of bulk materials,[108,113] the rebonding between otherwise intact fragments is particularly beneficial in the optimization of large structures. To examine the effectiveness of this operation in the case of NPs, we considered two related crossover and mutation operations. The first one is crossover performed with a spherical cut that seems more natural for cluster geometries (Fig. 2(d)). The second one mimics the Rubik's cube rotation by a random angle along a planar cut that divides a single parent structure into two roughly equal hemispheres (Fig. 2(b)).

Panels (a–c) in Fig. 3 show the performance of the three operations for elemental Cu, Pd, and Ag clusters. In these tests, we used 50-member populations and limited the search to 200 generations to illustrate the different success rates for affordable search durations in the following NN-based runs. New structures were created with 70% of the titled operation as the primary driver to explore different PES basins, 20% of simple distortions to help locate nearby minima, and 10% of random NP generation to inject diverse starting points. The planar cut

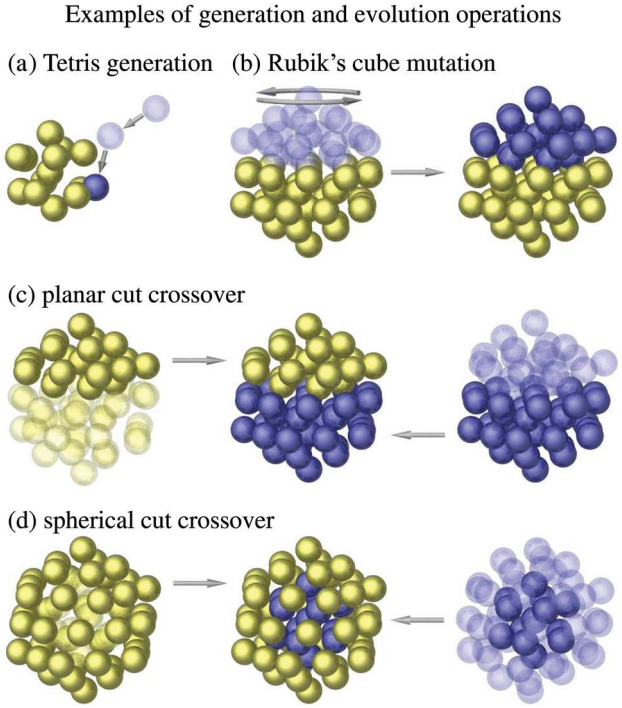

Fig. 2 Illustration of generation and evolution operations for elemental NPs. The semitransparent spheres represent atoms that are being added, rearranged, or discarded. The yellow and blue colors correspond either to fixed and repositioned atoms or to NP fragments from two different parents. (a) Addition of a new atom in a Tetris-like creation of random NPs. (b) Rubik's cube rotation of the NP's top half by a random angle. (c and d) Crossover performed with either planar or spherical cuts.

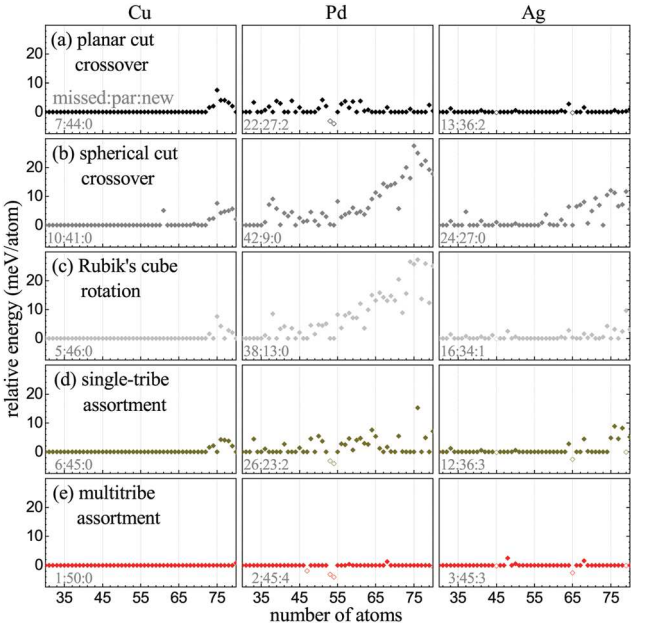

Fig. 3 Comparison of different evolutionary search strategies for elemental Cu, Pd, and Ag NPs modeled with the GP. (a–c) Single-tribe optimization with the titled operation used to create 70% of offspring. (d) Single-tribe optimization with a balanced assortment of various operations described in the main text. (e) Multitribe co-evolutionary optimization with the same operation assortment. The best structures found in each run are compared against the putative ground states proposed by Wu *et al.*[22] Identified lower-energy structures are shown with hollow symbols.

crossover performed better for Cu and Ag than for Pd, missing 7, 13, and 22 of the previously reported lowest-energy structures, respectively. Interestingly, the search identified 2 Pd structures lower in energy by 3–4 meV per atom compared with the reference set (Section 4). The success rate dropped considerably in the case of the spherical cut crossover, especially for Pd and Ag. We ensured that the boundary between fragments had meaningful interatomic distances, but it was evident that the core–shell combination either carried less significant information from each parent or could not be optimized into a seamless stable shape with local relaxations. This conclusion is supported by the operation's particularly poor performance for Pd, as this metal adopts a variety of less spherical stable structures (Section 4). The Rubik's cube mutation was found to be comparable to the planar cut crossover for Cu and Ag, having missed only 5 and 16 structures, respectively. Hence, the optimization of Cu and Ag clusters with simpler geometries appears to be less sensitive to how the fragments are recombined as long as they are obtained by bond-breaking planar cuts. The subpar performance of the Rubik's cube rotation for Pd indicates that the inheritance of phenotypes from two different parents is more important than the mutation of a single parent when dealing with more complex shapes.

We implemented additional single-parent mutation operations that could locate specific global minima more efficiently. Since faceting is known to reduce surface energy in large NPs, we introduced an operation that promotes the formation of facets in random directions. In this procedure, about $\sqrt{N}$ atoms are selected with a single planar cut and relocated to random positions on the opposite side. Since stable NPs also tend to possess symmetries, we considered two simple symmetrization operations. In both, a single parent structure is sliced into two nearly equal hemispheres, and the smaller part is discarded. The full NP is then regenerated from the remaining part using either reflection or inversion. Any two atoms of the same species that happen to be close to each other are merged into one, and the child structure is accepted if the cluster has the proper number of each species. According to our tests (not shown), these three operations showed efficiencies comparable to that of the Rubik's cube mutation.

Having tested multiple combinations, we ultimately chose to use a balanced assortment of several implemented operations. Each of the planar cut, spherical cut, Rubik's cube rotation, facet mutation, reflection mutation, inversion mutation, and random atom distortion operations was used to generate 10% of offspring. The remaining 30% of child structures were created with a redistribution of surface atoms in randomly selected parents; this operation was generalized in multitribe optimizations to exchange variable-size seeds (see Section 3.3). Results in Fig. 3(d) illustrate that the search produced a set of low-energy structures comparable to that found with the planar cut crossover including several additional putative ground states for Pd and Ag.

3.3 Multitribe co-evolution

Examples in different fields, from finding a cooperative relationship between populations of bacteria in biological systems[114,115] to solving for optimal load distribution in parallel computing systems,[116] demonstrate the benefits of optimization achieved *via* the use of multiple co-evolving tribes. In this evolutionary process commonly seen in Nature, individual tribes develop specific traits in isolation and periodically interact with neighboring tribes. The two major types of interactions are competition, which subjects the combined population to 'survival of the fittest' evolutionary pressure, and cooperation, which leads to an intertribe exchange of genetic material.

Several adaptations of this co-evolution strategy have been used to improve structure prediction. Habershon *et al.* found ordered crystalline phases consistent with experimental powder diffraction data more efficiently by defining a global population of structures and redistributing members among individual tribes every few generations.[117] In all other variations of the parallel evolutionary optimization, a single pool or population of structures has been used to explore the configuration space by varying composition/size at the same time.[113,118–120] For instance, the simultaneous optimization of bulk binary phases[113,118] relied on the distance to the convex hull as the fitness parameter for phases across the full composition range, while crossover operations allowed the creation of child structures with differing stoichiometries. The global variable-size/composition optimization approach has been shown to have a clear advantage over the independent optimization of fixed-size/composition crystalline phases[113,118] or NPs.[119,120]

The algorithm for simultaneous optimization of NPs across different sizes introduced in this study divides the global population into distinct tribes and imposes periods of isolated evolution. The schematic in Fig. 4(a) illustrates the flow of information during such global searches. We assigned one tribe per NP size and optimized the combined population in cycles of five-generation isolated evolution followed by an intertribe exchange of structural motifs. The pool of geometries used to seed a new cycle consisted of 15 structures, with 8 neighboring sizes contributing the most stable NP from the previous cycle, and the remainder comprising NPs chosen randomly from the previous generation of the NP size. We removed or added surface atoms to match the targeted size and optionally distorted $\sim\sqrt{N}$ atoms on the NP surface. The co-evolutionary method could be expected to be more efficient due to the persistence of certain stable motifs over multiple sizes. For example, the 55-atom icosahedron shown in Fig. 4(b) is the well-known ground state for several metals, and most algorithms find the structure relatively quickly because it is highly symmetric and stable. Derivatives of this motif with missing or added atoms may also be the ground state for neighboring sizes but are more difficult to find because of the reduced symmetry and stability. Namely, without a clear edge over competing configurations, the icosahedron-based precursors have a lower chance of survival and are less prevalent in populations with non-ideal cluster sizes. The intertribe exchange and minor adjustment of already assembled stable shapes could help the tribes to shortcut directly to the most stable solutions.

In our benchmark multitribe runs with the GP, we used the same assortment of operations as in single-tribe searches.

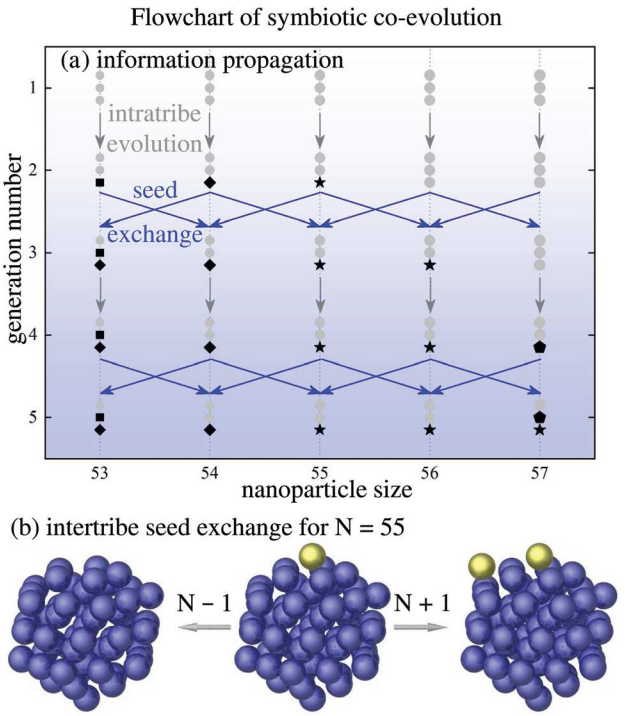

Fig. 4 (a) Schematic of the multitribe co-evolutionary optimization. The global population is divided into tribes by NP size and evolved in a cyclic fashion. Each cycle involves tribes' isolated evolution for a few generations followed by an exchange of best members among several tribes of neighboring NP sizes. Particularly stable motifs, *e.g.*, the diamond shape for $N = 54$, have a chance to spread over the global population and morph into ground states for other NP sizes. (b) Illustration of the NP size adjustment during intertribe seed exchange.

A dramatic improvement in the success rate was observed using this flavor of the evolutionary optimization (see Fig. 3(e)). Out of the 153 Cu, Pd, and Ag cases, only 6 reference structures were missed by 0.3–2.5 meV per atom and 7 new structures were identified to be more stable by 0.1–4.1 meV per atom. Two of the new Pd putative ground states were incomplete icosahedra with a missing center atom (for $N = 54$) or missing center and surface atoms ($N = 53$). The finding highlights the benefit of sharing seeds across NP sizes and the need to sample counter-intuitive configurations, as one might expect a smaller energy penalty for removing an atom from the surface rather than the middle of a metallic NP. Considering the $\sim$10 meV per atom accuracy of our NN models, the implemented search algorithm and the chosen settings deliver an appropriate level of convergence for a systematic comparison of the NN and GGA accuracy for low-energy structures.

4 Results and discussion

4.1 Review of previous work

The most systematic GP-based study of metallic NPs has been recently performed by Wu *et al.*[22] They utilized the dynamic lattice searching method and found that the main structural motifs of the Cu, Pd, and Ag NPs between 13 and 100 atoms in size are the icosahedron, decahedron, and icosahedron/decahedron, respectively. Their analysis of the PES for the intermediate-size 38-atom NPs showed that the number of the local minima, and hence the PES complexity, increases in the order of Pd, Ag, and Cu.[22]

In the binary subsystems of the Cu–Pd–Ag ternary, systematic GP-based ground state searches have been mostly restricted to select magic sizes.[7] For Cu–Ag bimetallic NPs, the lowest formation energy configurations have been shown to have Cu–Ag core–shell ordering and occur in the 0.6–0.8 Ag-rich composition range. Namely, the most stable magic-size clusters with 34, 38, 40, and 98 atoms have been found to have 27,[61] 29[78] or 30,[61] 27,[63] and 58–64[78] Ag atoms, respectively. The smaller clusters commonly adopt polyicosahedral core–shell configurations, while the 98-atom NPs assume structures with icosahedral Cu cores and (anti-)Mackay Ag overlayers. Considerable atomic size mismatch of Cu and Ag, bond order-bond length correlation, lower surface energy of Ag, dominance of Cu–Cu and Cu–Ag bonds, and HOMO–LOMO gap have been suggested as important factors in determining the structure of the energetically favored nanoalloys.[61,63–65] Global optimizations of Pd–Ag bimetallic NPs with 34 and 38 atoms have revealed that the lowest formation energy structures occur at stoichiometries with 24,[66] and 24[67] or 26[66] Ag atoms, respectively. As in the Cu–Ag case, Ag atoms prefer to be in the outer layers of stable NPs. However, the smaller atomic size difference of Pd and Ag evidently leads to a less pronounced segregation tendency and a lower favorability of the polyicosahedral motif.[66]

4.2 Elemental nanoparticles

We employed the multitribe co-evolution algorithm (Section 3.3) and our developed NN models (Section 2.3) to search for stable Cu, Pd, and Ag elemental NPs with 30–80 atoms. Such clusters are large enough not to be dominated by electronic structure peculiarities associated with low-coordination atomic environments that are difficult to capture with classical models. At the same time, the clusters are small enough to be systematically explored with NNs and checked with DFT. Even though clusters of these sizes are of little practical value, they can be synthesized experimentally[121] and may be used as a testing ground for checking theoretical predictions. A typical global optimization run consisted of 100–200 generations with a population size of 50 structures per tribe. For Ag and Pd, as higher NN residual errors suggest, the PES is more complicated. We performed two multitribe searches for these metals and selected the lowest energy structures for each size.

Fig. 5 illustrates the stability of these structures relative to the putative ground states proposed by Wu *et al.*[22] The comparison was done at the GGA and LDA levels and involved energy evaluations of the structures relaxed locally with either the corresponding classical model (hollow points) or the corresponding DFT approximation (solid points). The results indicate that between the candidate structures identified with the GP and NN models, the latter are consistently more stable at the DFT level for all three metals. The figure also reveals the NN's good agreement with the GGA in evaluating forces, as the GGA-level re-optimization of the NN-relaxed structures led to

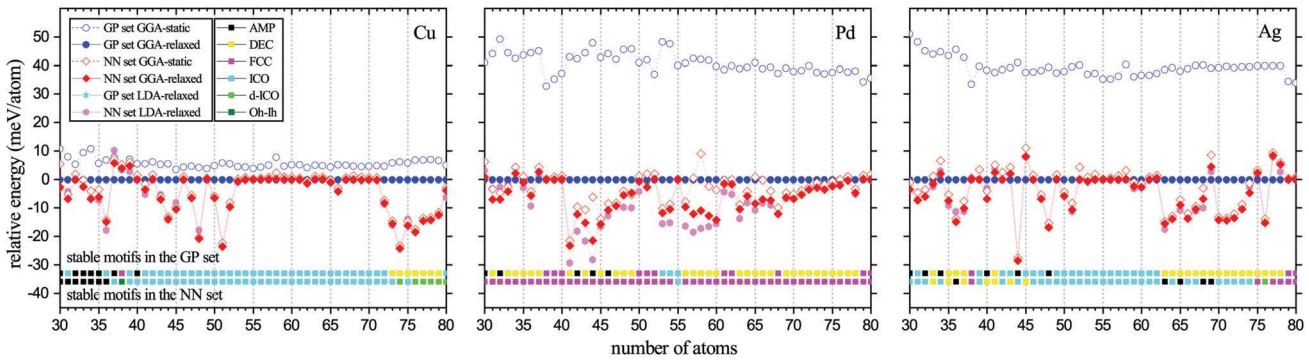

Fig. 5 Relative stability evaluated at the DFT level for two NP sets: the lowest-energy structures identified in our NN-based multitribe searches and the putative ground states found previously in GP-based dynamic lattice searches.[22] The solid points correspond to structures locally relaxed with GGA or LDA. The GP DFT-relaxed structures are used as a reference in the calculation of the relative energies. The hollow points correspond to the GGA relative energies for the original unrelaxed structures in the GP or NN sets. The two strings of color-coded square symbols show significantly different distributions of stable structural motifs in the two NP sets.

energy gains of only a few meV per atom. The structures found with the NN-model underwent a-common nearest neighbor analysis[122] (a-CNA) to describe the local environment of each atom in terms of well-known reference structures. The structures were then classified manually based on their visual similarity to the motifs used to describe NPs in ref. 22.

The NN-based search for Cu NPs resulted in 26 new minima. In the N = 30–60 range, several structures are significantly more stable than those found through GP-based searches, by 10 meV per atom or more (Fig. 5) at the GGA level. Most of these energy gains are not the result of substantially different configurations but rather different decorations of incomplete icosahedron shapes. For N = 36, the change does result in an amorphous (AMO) structure that resembles a distorted incomplete icosahedral structure.

For N = 38, the NN favored a mixed octahedral–icosahedral (O_h–I_h) structure; although this motif has been reported to be a low-energy isomer in other elemental[123] and binary[124] systems, our GGA calculations placed it 3.9 meV per atom above the GP-favored FCC structure for Cu. The most striking improvements over the results reported for Cu in ref. 22 and 125 occur in the N = 72–80 range. The previously reported minima show an icosahedral (ICO) trend up to N = 72 with a switch to decahedral (DEC) motif up to N = 79, and finally an ICO shape for N = 80. The competing morphologies of structures identified in our search in this size range are the typical ICO with an (anti)-Mackay layer (N = 72, 73, and 75) and double icosahedrons (d-ICO) (N = 74 and 76–80). The DEC shapes previously reported in ref. 22 are not observed to be stable at the GGA level. The d-ICO shape first appears at N = 74 with a disordered arrangement. Further occurrences of d-ICO at larger sizes show a more ordered configuration for N = 78 and 80 (Fig. 6).

Searches for Pd NPs produced 41 new minima at the GGA level. The morphologies of the new configurations represent a significant departure from what was previously reported.[22,77] The motifs reported included DEC, ICO, stacking-fault face-centered cubic (sf-FCC), and AMO motifs. The DEC motif was found to be dominant throughout the N = 30–80 range.[22,77] Our results, however, show that the face-centered cubic (FCC) structures are more stable at the GGA level than other shapes throughout most of the examined range. The stable FCC motifs shown in Fig. 5 include truncated octahedra (O_h), which were found for N = 38 and 79 in agreement with previous results,[22] and an octahedron, which was found to be a minimum for N = 44 (Fig. 6). The new minima also include three sf-FCC NPs for N = 35, 36, and 51. The preference for the FCC shape has been attributed to the generalized Wulf construction principle.[126] A notable exception to the FCC trend is the magic ICO shape found for N = 55. Piotrowski *et al.*[58] determined the FCC to be the preferred motif for Pd by 3.8 meV per atom at the GGA level with the PAW-GW pseudopotential and a 250 eV energy cutoff. In our PAW-GGA calculations with the 500 eV cutoff, the ICO and FCC motifs were found to be within 0.1 meV per atom. The juxtaposition illustrates that the NN model's misevaluation of the relative stability of the two motifs by 3.7 meV per atom in favor of the former is not only well within the NN's 8.6 meV per atom test error but also comparable to the typical calculation errors in the same DFT approximation.

The NN-based search for Ag NPs uncovered 27 new minima compared to the reference structures[22] at the GGA level. Similar to our results for Cu, most of the new putative global minima for structures of 60 atoms and below are variations of the incomplete ICO morphology (Fig. 5). The largest gain in energy in this size range was for size N = 44, which in ref. 22 was found to be an ICO-like amorphous (AMP) structure and in our study an incomplete ICO motif with an energy gain of almost 30 meV per atom at the GGA level. We found that the competition between ICO and ICO-like AMP motifs occurs in the N = 63–69 size range. For the N = 70–74 and 76 sizes, the DEC morphology found in ref. 22 and 127 was replaced with (anti)-Mackay ICO structures at the GGA level.

Fig. 5 shows that only 13 (~8.5%) of the elemental reference structures[22] were not matched or improved upon at the GGA level, whereas 96 (~62.7%) were found to be new putative global minima at the GGA level. This performance evaluation of the two classical models is understandably biased because the

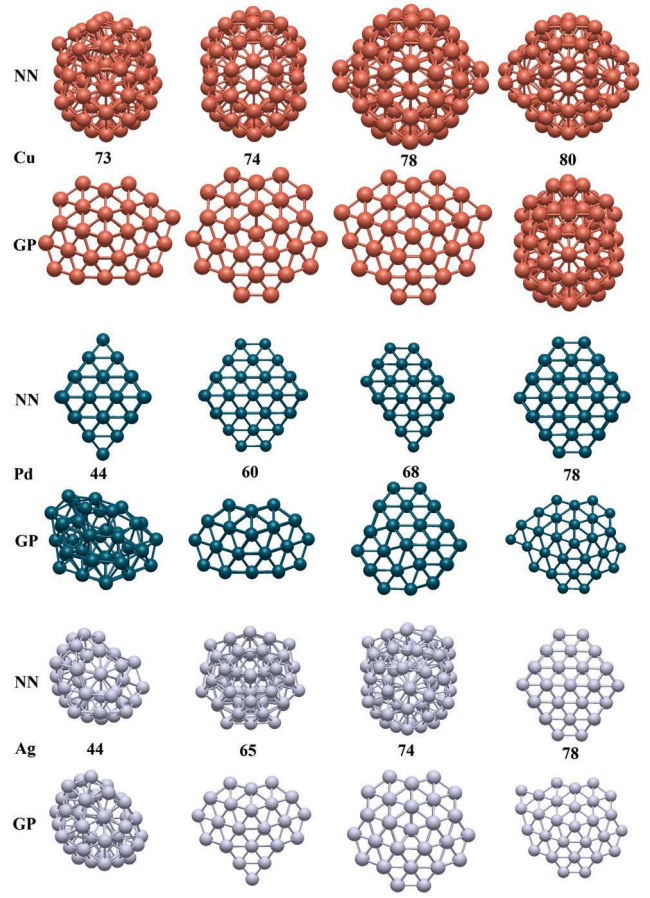

Fig. 6 Examples of significantly different structural motifs favored by the NN and GP models. The relative stability and structure classification for Cu, Pd, and Ag NPs in the N = 30–80 size range are presented in Fig. 5.

NNs were trained on GGA data, while the GPs were fitted to empirical data. Considering that the GPs showed much better agreement with the LDA in the description of forces for Pd and Ag (see Fig. 1), we examined the relative stability of the structures in the NN and GP pools at the LDA level as well. Remarkably, the structures favored by the NNs remained consistently more stable in the LDA treatment, as the relative energies evaluated in the two DFT approximations matched reasonably well (Fig. 5).

Another comparison of the classical models' ability to map the GGA PES is illustrated in Fig. S6 (ESI†). We selected several metastable 55-atom structures from the NN and GP pools and evaluated their relative energies with single-point GGA calculations. The NN models provided a much more consistent energy ordering than the GPs within the chosen 20 meV per atom window above the corresponding ground states.

The energy gains in GGA optimization of NN and GP best structures in Fig. 5 provide useful information about the PES features. Indeed, significant structural relaxations could be a contributing factor to the suboptimal stability of the resulting minima. The argument is based on an expectation that the longer the trajectories the higher the chance for structures to get trapped in nearby local minima. For the considered metals, the energy gains in GGA relaxations of the GP structures were notably different: about 10 meV per atom for Cu and 40 meV per atom for Pd/Ag. Nevertheless, the GP-derived minima ended up above NN-derived minima by a similar 10 meV per atom for all three metals. These results suggest that the GGA basins around the starting GP configurations are smooth. The conclusion is supported by the analysis of the NP estimated volumes (defined in ref. 90) before and after the relaxation. It reveals an overall expansion of the GP structures in the GGA optimizations by 0.0% for Cu, 2.2% for Pd, and 3.2% for Ag. Hence, the starting geometry appears to be of less significance than the ranking of the relevant basins for identifying global DFT minima with these classical models.

We also assessed the contribution of the vibrational entropy on the relative stability of the NN and GP best structures at elevated temperatures. Our previous tests showed a good agreement between the NN and DFT results for phonon dispersions and vibrational entropy corrections to the free energy calculated in Cu–Pd–Ag[36] and Mg–Ca[40] bulk phases. Here, we used the NN models to examine 33 NP pairs with 30–80 atoms and found that the relative free energies at 300 K changed on average by only 0.7, 2.7, and 1.9 meV per atom for Cu, Pd, and Ag, respectively. Therefore, most of the NPs in the NN pool determined at T = 0 K to be more stable than those in the GP pool are expected to be more stable at elevated temperatures as well. A comprehensive analysis of the NP stability at high temperatures involves long MD simulations or a systematic sampling of local minima[128,129] and will require a separate study.

4.3 Binary nanoparticles

We investigated the stability of binary nanoalloys for several representative NP sizes (50, 55, and 80 atoms) by performing NN-based single-tribe evolutionary searches for select stoichiometries. We sampled the binary compositions in steps of 5 atoms for the two smaller sizes and in steps of 10 atoms for the largest size to identify regions with low formation energies. The similar-size NPs with 50 and 55 atoms were considered to compare stability trends in cases of low-symmetry and high-symmetry configurations, as the NNs favored different-shape and same-shape elemental ground states for the three metals, respectively. The larger 80-atom NPs were examined to assess the importance of size effects. The searches were carried out using the same set of evolutionary operations as in the case of single elements with the addition of atom swaps in the mutation operations. Because of the more complex nature of the PES for binary NPs, we extended the searches to 500 generations and executed two separate runs. The resulting lowest-energy NPs with 50 and 55 atoms were reoptimized at the GGA level. While thermodynamically stable bulk alloys are determined unambiguously by calculating Gibbs formation energies and constructing the convex hull,[109] the variability of NP sizes governed by a combination of kinetic and thermodynamic factors greatly complicates the stability analysis. We used a common measure of the nanoalloy stability based on the formation energy.[63,67] For an A–B binary NP with

$N = N_A + N_B$ atoms, the formation energy per atom is calculated with respect to the most stable elemental NPs, each of size N, as follows:

$$E_{AB}^{form} = E_{AB} - \frac{N_A}{N_A + N_B}E_A - \frac{N_B}{N_A + N_B}E_B,$$

where E_{AB}, E_A, and E_B represent the energies per atom of the $(N_A + N_B)$-atom binary and elemental clusters, respectively. As argued by Ferrando *et al.*,[130] the reliance on the NP rather than bulk ground states as references helps avoid element-dependent bias when comparing clusters of the same size but different compositions. Given that the NP ground states in this study were determined with a 10 meV per atom accuracy, we could not determine the boundary of the convex hull definitively to identify the full set of stable nanoalloys in the considered multicomponent systems. We will refer to most stable compositions as stoichiometries corresponding to the lowest formation energies.

Fig. 7 summarizes formation energy results for 50-atom NPs and illustrates that the most stable binary compositions identified in our NN-based searches are $Cu_{0.6}Pd_{0.4}$, $Cu_{0.3}Ag_{0.7}$, and $Pd_{0.3}Ag_{0.7}$. The Cu–Pd NPs adopt an incomplete ICO shape at the Cu-rich end, become disordered at the $Cu_{0.5}Pd_{0.5}$ composition, and assume incomplete anti-Mackay ICO or incomplete-sixfold pancake structures at the Pd-rich end. The Cu–Ag putative ground states have Ag-rich polyicosahedral shapes such as the anti-Mackay ICO and incomplete pancake structures. Interestingly, the Pd–Ag ground state NPs are mostly different incomplete ICO structures (with the exception of FCC-type $Pd_{0.9}Ag_{0.1}$) despite the reference structures for Pd and Ag being FCC and incomplete ICO, respectively.

In order to evaluate the degree and importance of mixing in stable NPs we compared the number of total and interspecies neighbors within 3.2 Å in the lowest-energy NPs at the 1 : 1 composition. Out of 207, 219, and 205 total bonds in the corresponding CuPd, CuAg, and PdAg 50-atom NPs, 103, 82, and 92 were between different metals. The results at this and other compositions are consistent with the largest (smallest) magnitudes of the formation energy observed in the Cu–Pd (Cu–Ag) nanoalloys. As for the dependence of the bimetallic NP stability on the size and/or structure, Table 4 summarizes the stoichiometries with the lowest formation energies in all considered cases. The results show that it is difficult to draw any definitive conclusions regarding possible correlations because the variations in stable compositions are comparable to the chosen grid sizes (Fig. S7, ESI†).

Table 4 NN- and GGA-level composition ratio (x in $A_{1-x}B_x$) and formation energy (E_{form}) (in meV per atom) corresponding to the most stable binary NPs with 50, 55, and 80 atoms

		Cu–Pd		Cu–Ag		Pd–Ag	
Cluster size		x	E_{form}	x	E_{form}	x	E_{form}
50 atoms	NN	0.40	−140.5	0.70	−72.5	0.70	−131.8
	GGA	0.40	−132.6	0.80	−35.5	0.70	−125.8
55 atoms	NN	0.45	−156.1	0.73	−59.5	0.64	−136.2
	GGA	0.36	−148.4	0.73	−32.0	0.55	−121.5
80 atoms	NN	0.37	−123.8	0.62	−71.6	0.62	−113.2

We also performed comparative ground state searches with the available Cu–Ag and Pd–Ag GPs.[74] Reoptimization of these 18 50-atom NPs with the GGA resulted in 6 structures of lower energy (by an average of 2.6 meV per atom) and 12 structures of higher energy (by an average of 14.7 meV per atom) compared to the NN-based set (Fig. 7). Formation energies of the NN- and GP-based sets, evaluated by GP, NN, and GGA are detailed in Fig. S8 (ESI†). Despite the overall suboptimal performance, the GPs were accurate enough to suggest candidate structures for reasonable GGA estimates of the stability regions and formation energies. However, as in the case of the elemental NPs (Section 2.4), the GPs showed less agreement with the GGA in the description of atomic forces: the RMSEs were 0.20 and 0.33 eV $Å^{-1}$ for the lowest-energy Cu–Ag and Pd–Ag NPs, respectively. The NNs described the forces with a considerably better accuracy: 0.05, 0.04, and 0.06 eV $Å^{-1}$ for the corresponding sets of lowest-energy Cu–Pd, Cu–Ag, and Pd–Ag NPs.

4.4 Ternary nanoparticles

Ternary Cu–Pd–Ag nanoalloys have not been studied previously either at the classical or the DFT level. Our searches for putative ground states of 50-, 55-, and 80-atom ternary NPs were performed with the same settings as in the case of binary

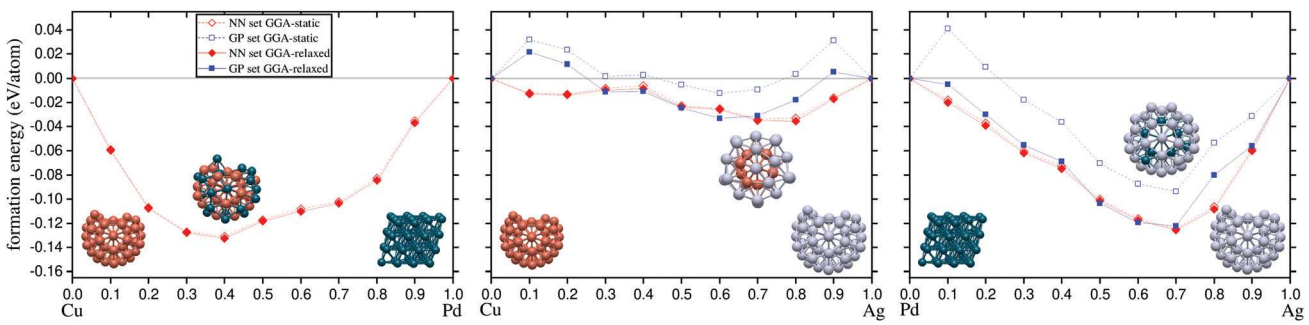

Fig. 7 GGA formation energies of most stable 50-atom bimetallic NPs found in our evolutionary searches at the NN (red points) and GP (blue points) levels. The hollow and solid symbols correspond to GGA evaluations of the non-modified and GGA-optimized putative ground states, respectively. Each panel shows the most stable elemental and binary structures found in the NN-based searches.

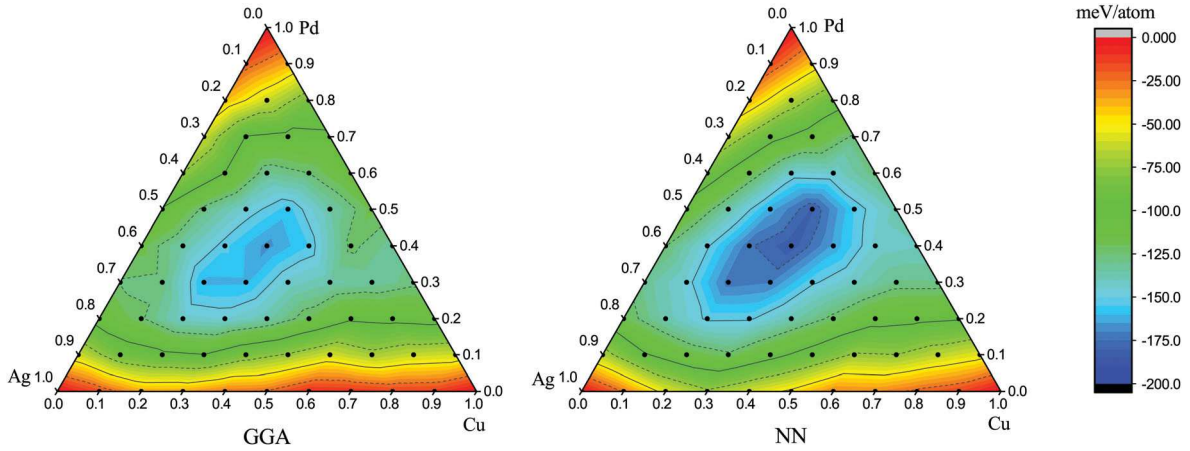

Fig. 8 Color-coded formation energies calculated at the GGA (left) and NN (right) levels for putative ground states of 50-atom Cu–Pd–Ag NPs found in our NN-based evolutionary searches. All the structures were relaxed with the corresponding GGA or NN method.

nanoalloys. Within the sampled grid, a 50-atom ternary cluster with the lowest formation energy was found at the $Cu_{0.3}Pd_{0.4}Ag_{0.3}$ composition (Fig. 8) and displayed an incomplete six-fold pancake structure with a Cu core and Pd–Ag shell. The NP also had the lowest GGA formation energy when the full set of putative ground states was reoptimized in this DFT approximation. Note that the higher $\sim$20 meV per atom discrepancy between the NN and GGA results in Fig. 8 is consistent with the accumulation of errors in the calculation of ternary formation energies referenced to the elemental NP ground state energies. Overall, Fig. 8 shows an encouraging level of agreement between the NN and the GGA, as the NN model reproduces the stability trends and correctly identifies the island of NP stability.

Fig. S9 and S10 (ESI†) summarize our NN and DFT results on the formation energies for 50-, 55-, and 80-atom ternary NPs. We did not observe any significant dependence of the lowest formation energy stoichiometry on the NP size. According to the NN modeling, the optimal ternary compositions for nanoalloys with 55 and 80 atoms are $Cu_{0.272}Pd_{0.364}Ag_{0.364}$ and $Cu_{0.25}Pd_{0.375}Ag_{0.375}$, respectively. The GGA optimization of the 55-atom NPs confirms the NN model's findings (Fig. S9, ESI†). These observations provide further support for future use of NNs as a reliable stand-alone method for describing large-scale systems.

5 Summary

This work has been dedicated to the development, examination, and application of computational methods for predicting stable NPs.

Aiming to improve ground state search efficiency, we introduced a multitribe evolutionary algorithm for simultaneous optimization of NPs in a specified size range. In contrast to previously implemented variable-size/composition global optimization strategies, our approach features well-defined periods of isolated evolution for individual tribes followed by intertribe seed exchange. This symbiotic co-evolution scheme showed a clear advantage over the conventional serial evolutionary optimization of fixed-size NPs. In our relatively short 200-generation benchmark runs with 50-member tribes of Cu, Pd, and Ag NPs in the 30–80 atom range, the multitribe searches identified 7 new putative ground states at the GP level compared to previously reported candidate structures.

Given the lack of systematic studies comparing the reliability of NN models and empirical potentials in ground state searches, we performed benchmark tests of NN and GP models against DFT approximations for elemental and binary NPs. The Cu–Pd–Ag NN models were constructed from the bottom up and showed a consistent $\sim$10 meV per atom accuracy for nanoalloys, which illustrates that our stratified training scheme originally tested on bulk structures is applicable to datasets with more complex NP configurations. The lowest-energy structures identified in our searches at the NN and GP levels were evaluated without and with relaxation at the GGA level. Between the NNs fitted to GGA data and the GPs fitted to empirical data, the former showed an expectedly better agreement with this DFT approximation. In terms of the quality of the atomic force description, most of the NN (GP) configurations were found to be within about 4 (40) meV per atom of the nearest minima on the GGA PES.

In terms of the total energy correspondence, the GP candidate structures were favored by the GGA in 8.5% of considered cases by an average of 4.2 meV per atom while the NN ones in 62.7% by an average of 9.1 meV per atom, with 26.1% of the NN pool by more than 10 meV per atom. According to our additional LDA calculations, all the putative ground states from the NN pool favored by the GGA were also favored by the LDA. The findings indicate that the NNs provide a more reliable mapping of the DFT PES. Comparative analysis of structures found in the NN- and GP-based searches revealed significant changes in the previously discussed stability trends. For example, we found the largest elemental NPs to be more stable in ICO/d-ICO rather than DEC morphologies for Cu, FCC rather than DEC for Pd, and ICO rather than DEC for Ag.

We would like to note that due to the wide scope of the study and the high cost of DFT calculations we considered only one

best structure per size or composition from each of the GP and NN pools, which is certainly insufficient for determining the true GGA ground states. However, it should also be pointed out that the typical $\sim$3 meV per atom level of ground state search convergence and $\sim$10 meV per atom NN accuracy are comparable to the 3 meV per atom DFT numerical errors (*e.g.*, found in this study for Pd_{55}) and $\sim$10 meV per atom DFT systematic errors[107,131–133] (found to be $\sim$3 meV per atom for select NPs in Table S1, ESI†). These observations highlight the difficulty of establishing definitively which stable NP configurations occur in experiments even if none of the numerous environmental factors are considered. Namely, free energy corrections due to entropy, kinetic effects, influence of solutions and substrates, *etc.*, must be evaluated at target temperatures with sufficient accuracy, which presents a much greater challenge compared to the identification of putative ground states at zero temperature performed in this study.[128] Nevertheless, the NN/DFT level of accuracy may allow one to identify regions of zero-temperature nanoalloy stability. According to our analysis of bimetallic systems, GP-based candidate structures are still generally inferior to those found with NNs but can be used for an adequate prediction of most stable stoichiometries. The following NN/DFT examinations of medium-size ternary Cu–Pd–Ag NPs revealed that NNs are sufficiently accurate for predicting "regions" that most likely contain stable nanoalloy(s). These results suggest that NN models can be used for a reliable simulation of nanoscale materials that are too large for full-scale DFT calculations.

Conflicts of interest

There are no conflicts to declare.

Acknowledgements

The authors thank Javier Rojas-Nunez and Samuel E. Baltazar for valuable discussions and acknowledge the NSF support (Award No. DMR-1821815).

References

1 N. Sharma, H. Ojha, A. Bharadwaj, D. P. Pathak and R. K. Sharma, *RSC Adv.*, 2015, **5**, 53381–53403.
2 S. K. Verma and A. K. Tiwari, *Mater. Today: Proc.*, 2015, **2**, 3638–3647.
3 O. V. Salata, *J. Nanobiotechnol.*, 2004, **2**, 1–6.
4 R. L. Johnston, *J. Chem. Soc., Dalton Trans.*, 2003, **3**, 4193–4207.
5 S. Heiles and R. L. Johnston, *Int. J. Quantum Chem.*, 2013, **113**, 2091–2109.
6 G. Rossi and R. Ferrando, *J. Phys.: Condens. Matter*, 2009, **21**, 84208.
7 F. Baletto, *J. Phys.: Condens. Matter*, 2019, **31**, 113001.
8 S. M. Woodley, A. A. Sokol and C. R. A. Catlow, *Z. Anorg. Allg. Chem.*, 2004, **630**, 2343–2353.
9 D. Daven, N. Tit, J. Morris and K. Ho, *Chem. Phys. Lett.*, 1996, **256**, 195–200.
10 C. Barrón, S. Gómez, D. Romero and A. Saavedra, *Appl. Math. Lett.*, 1999, **12**, 85–90.
11 S. E. Schönborn, S. Goedecker, S. Roy and A. R. Oganov, *J. Chem. Phys.*, 2009, **130**, 144108.
12 D. J. Wales and J. P. Doye, *J. Phys. Chem. A*, 1997, **101**, 5111–5116.
13 H. G. Kim, S. K. Choi and H. M. Lee, *J. Chem. Phys.*, 2008, **128**, 144702.
14 D. J. Wales and H. A. Scheraga, *Science*, 1999, **285**, 1368–1372.
15 S. Goedecker, *J. Chem. Phys.*, 2004, **120**, 114105.
16 X. Shao, L. Cheng and W. Cai, *J. Comput. Chem.*, 2004, **25**, 1693–1698.
17 X. Shao, X. Yang and W. Cai, *J. Comput. Chem.*, 2008, **29**, 1772–1779.
18 X. Wu, W. Cai and X. Shao, *Chem. Phys.*, 2009, **363**, 72–77.
19 S. T. Call, D. Y. Zubarev and A. I. Boldyrev, *J. Comput. Chem.*, 2007, **28**, 1177–1186.
20 J. Lv, Y. Wang, L. Zhu and Y. Ma, *J. Chem. Phys.*, 2012, **137**, 84104.
21 C. J. Pickard and R. J. Needs, *J. Phys.: Condens. Matter*, 2011, **23**, 053201.
22 X. Wu and Y. Sun, *J. Nanopart. Res.*, 2017, **19**, 201.
23 Y. Nanba, T. Ishimoto and M. Koyama, *J. Phys. Chem. C*, 2017, **121**, 27445–27452.
24 D. Selli, G. Fazio and C. Di Valentin, *Catalysts*, 2017, **7**, 357.
25 H. Zhang, D. Tian and J. Zhao, *J. Chem. Phys.*, 2008, **129**, 114302.
26 A. S. Chaves, M. J. Piotrowski and J. L. Da Silva, *Phys. Chem. Chem. Phys.*, 2017, **19**, 15484–15502.
27 G. Csányi, T. Albaret, M. C. Payne and A. De Vita, *Phys. Rev. Lett.*, 2004, **93**, 175503.
28 S. Y. Chen, F. Zheng, S. Q. Wu and Z. Z. Zhu, *Curr. Appl. Phys.*, 2017, **17**, 454–460.
29 J. Behler and M. Parrinello, *Phys. Rev. Lett.*, 2007, **98**, 146401.
30 W. J. Szlachta, A. P. Bartók and G. Csányi, *Phys. Rev. B: Condens. Matter Mater. Phys.*, 2014, **104108**, 1–6.
31 S. Kondati Natarajan, T. Morawietz and J. Behler, *Phys. Chem. Chem. Phys.*, 2015, **17**, 8356–8371.
32 N. Artrith, B. Hiller and J. Behler, *Phys. Status Solidi B*, 2013, **250**, 1191–1203.
33 E. L. Kolsbjerg, A. A. Peterson and B. Hammer, *Phys. Rev. B*, 2018, **97**, 195424.
34 B. Onat, E. D. Cubuk, B. D. Malone and E. Kaxiras, *Phys. Rev. B*, 2018, **97**, 94106.
35 A. Khorshidi and A. A. Peterson, *Comput. Phys. Commun.*, 2016, **207**, 310–324.
36 S. Hajinazar, J. Shao and A. N. Kolmogorov, *Phys. Rev. B*, 2017, **95**, 14114.
37 V. L. Deringer, C. J. Pickard and G. Csányi, *Phys. Rev. Lett.*, 2018, **120**, 156001.
38 V. L. Deringer, N. Bernstein, A. P. Bartók, M. J. Cliffe, R. N. Kerber, L. E. Marbella, C. P. Grey, S. R. Elliott and G. Csányi, *J. Phys. Chem. Lett.*, 2018, **9**, 2879–2885.

39 V. L. Deringer, C. J. Pickard and G. Csányi, *Phys. Rev. Lett.*, 2018, **120**, 156001.
40 W. Ibarra-Hernández, S. Hajinazar, G. Avendaño-Franco, A. Bautista-Hernández, A. N. Kolmogorov and A. H. Romero, *Phys. Chem. Chem. Phys.*, 2018, **20**, 27545–27557.
41 N. Artrith, B. Hiller and J. Behler, *Phys. Status Solidi B*, 2013, **250**, 1191–1203.
42 J. R. Boes and J. R. Kitchin, *J. Phys. Chem. C*, 2017, **121**, 3479–3487.
43 S. Chiriki and S. S. Bulusu, *Chem. Phys. Lett.*, 2016, **652**, 130–135.
44 E. L. Kolsbjerg, A. A. Peterson and B. Hammer, *Phys. Rev. B*, 2018, **97**, 195424.
45 R. Ouyang, Y. Xie and D.-e. Jiang, *Nanoscale*, 2015, **7**, 14817–14821.
46 S. Chiriki, S. Jindal and S. S. Bulusu, *J. Chem. Phys.*, 2017, **146**, 84314.
47 S. Jindal, S. Chiriki and S. S. Bulusu, *J. Chem. Phys.*, 2017, **146**, 204301.
48 N. Artrith and A. M. Kolpak, *Comput. Mater. Sci.*, 2015, **110**, 20–28.
49 S. Chiriki, S. Jindal and S. S. Bulusu, *J. Chem. Phys.*, 2017, **147**, 154303.
50 J. Kang, S. H. Noh, J. Hwang, H. Chun, H. Kim and B. Han, *Phys. Chem. Chem. Phys.*, 2018, **20**, 24539–24544.
51 R. Ferrando, J. Jellinek and R. L. Johnston, *Chem. Rev.*, 2008, **108**, 845–910.
52 M. I. Din and R. Rehan, *Anal. Lett.*, 2017, **50**, 50–62.
53 M. B. Gawande, A. Goswami, F.-X. Felpin, T. Asefa, X. Huang, R. Silva, X. Zou, R. Zboril and R. S. Varma, *Chem. Rev.*, 2016, **116**, 3722–3811.
54 Q. H. Tran, V. Q. Nguyen and A. T. Le, *Adv. Nat. Sci.: Nanosci. Nanotechnol.*, 2013, **4**, 33001.
55 I. Saldan, Y. Semenyuk, I. Marchuk and O. Reshetnyak, *J. Mater. Sci.*, 2015, **50**, 2337–2354.
56 N. Zhang, F. Y. Chen and X. Q. Wu, *Sci. Rep.*, 2015, **5**, 11984.
57 Y. Xiong, W. Ye, W. Chen, Y. Wu, Q. Xu, Y. Yan, H. Zhang, J. Wu and D. Yang, *RSC Adv.*, 2017, **7**, 5800–5806.
58 M. J. Piotrowski, C. G. Ungureanu, P. Tereshchuk, K. E. A. Batista, A. S. Chaves, D. Guedes-Sobrinho and J. L. F. Da Silva, *J. Phys. Chem. C*, 2016, **120**, 28844–28856.
59 M. Chen, J. E. Dyer, K. Li and D. A. Dixon, *J. Phys. Chem. A*, 2013, **117**, 8298–8313.
60 K. Jug, B. Zimmermann, P. Calaminici and A. M. Köster, *J. Chem. Phys.*, 2002, **116**, 4497–4507.
61 G. Rossi, A. Rapallo, C. Mottet, A. Fortunelli, F. Baletto and R. Ferrando, *Phys. Rev. Lett.*, 2004, **93**, 105503.
62 A. Rapallo, G. Rossi, R. Ferrando, A. Fortunelli, B. C. Curley, L. D. Lloyd, G. M. Tarbuck and R. L. Johnston, *J. Chem. Phys.*, 2005, **122**, 194308.
63 G. Barcaro, A. Fortunelli, G. Rossi, F. Nita and R. Ferrando, *J. Phys. Chem. B*, 2006, **110**, 23197–23203.
64 M. Alcántara Ortigoza and T. S. Rahman, *Phys. Rev. B: Condens. Matter Mater. Phys.*, 2008, **77**, 195404.
65 H. Yildirim, A. Kara and T. S. Rahman, *J. Phys. Chem. C*, 2012, **116**, 281–291.
66 G. Rossi, R. Ferrando, A. Rapallo, A. Fortunelli, B. C. Curley, L. D. Lloyd and R. L. Johnston, *J. Chem. Phys.*, 2005, **122**, 194309.
67 X. Wu, Y. Wu, X. Kai, G. Wu and Y. Chen, *Chem. Phys.*, 2011, **390**, 36–41.
68 M. Chandross, *Modell. Simul. Mater. Sci. Eng.*, 2014, **22**, 75012.
69 S. Li, W. Qi, H. Peng and J. Wu, *Comput. Mater. Sci.*, 2015, **99**, 125–132.
70 V. I. Kuzmin, D. L. Tytik, D. K. Belashchenko and A. N. Sirenko, *Colloid J.*, 2008, **70**, 284–296.
71 J. P. K. Doye and D. J. Wales, *New J. Chem.*, 1998, **22**, 733–744.
72 W. Huang, X. Lai and R. Xu, *Chem. Phys. Lett.*, 2011, **507**, 199–202.
73 X. Lai, R. Xu and W. Huang, *J. Chem. Phys.*, 2011, **135**, 164109.
74 F. Baletto, C. Mottet and R. Ferrando, *Phys. Rev. B: Condens. Matter Mater. Phys.*, 2002, **66**, 1554201.
75 F. Cleri and V. Rosato, *Phys. Rev. B: Condens. Matter Mater. Phys.*, 1993, **48**, 22–33.
76 G. Rossi, G. Schiappelli and R. Ferrando, *J. Comput. Theor. Nanosci.*, 2009, **6**, 841–848.
77 X. Wu and Y. Dong, *New J. Chem.*, 2014, **38**, 4893–4900.
78 S. Núñez and R. L. Johnston, *J. Phys. Chem. C*, 2010, **114**, 13255–13266.
79 A. A. Peterson, *J. Chem. Phys.*, 2016, **145**, 74106.
80 K. Shakouri, J. Behler, J. Meyer and G. J. Kroes, *J. Phys. Chem. Lett.*, 2017, **8**, 2131–2136.
81 S. D. Huang, C. Shang, X. J. Zhang and Z. P. Liu, *Chem. Sci.*, 2017, **8**, 6327–6337.
82 Z. W. Ulissi, M. T. Tang, J. Xiao, X. Liu, D. A. Torelli, M. Karamad, K. Cummins, C. Hahn, N. S. Lewis, T. F. Jaramillo, K. Chan and J. K. Nørskov, *ACS Catal.*, 2017, **7**, 6600–6608.
83 J. P. Perdew, K. Burke, M. Ernzerhof and K. Burke, *Phys. Rev. Lett.*, 1996, **77**, 3865–3868.
84 D. C. Langreth and M. J. Mehl, *Phys. Rev. B: Condens. Matter Mater. Phys.*, 1983, **28**, 1809–1834.
85 P. E. Blöchl, *Phys. Rev. B: Condens. Matter Mater. Phys.*, 1994, **50**, 17953–17979.
86 G. Kresse and J. Hafner, *Phys. Rev. B: Condens. Matter Mater. Phys.*, 1993, **47**, 558–561.
87 G. Kresse and J. Furthmüller, *Phys. Rev. B: Condens. Matter Mater. Phys.*, 1996, **54**, 11169–11186.
88 M. Methfessel and A. T. Paxton, *Phys. Rev. B: Condens. Matter Mater. Phys.*, 1989, **40**, 3616–3621.
89 B. Hammer, L. B. Hansen and J. K. Nørskov, *Phys. Rev. B: Condens. Matter Mater. Phys.*, 1999, **59**, 7413–7421.
90 S. Chiriki, S. Jindal and S. S. Bulusu, *J. Chem. Phys.*, 2017, **146**, 84314.
91 R. Ouyang, Y. Xie and D. E. Jiang, *Nanoscale*, 2015, **7**, 14817–14821.
92 N. Artrith and A. M. Kolpak, *Comput. Mater. Sci.*, 2015, **110**, 20–28.
93 N. Artrith and A. M. Kolpak, *Nano Lett.*, 2014, **14**, 2670–2676.

94 J. P. Perdew and A. Zunger, *Phys. Rev. B: Condens. Matter Mater. Phys.*, 1981, **23**, 5048–5079.
95 R. P. Gupta, *Phys. Rev. B: Condens. Matter Mater. Phys.*, 1981, **23**, 6265–6270.
96 V. Rosato, M. Guillope and B. Legrand, *Philos. Mag. A*, 1989, **59**, 321–336.
97 F. Bianchini, J. R. Kermode and A. De Vita, *Modell. Simul. Mater. Sci. Eng.*, 2016, **24**, 45012.
98 A. N. Kolmogorov and V. H. Crespi, *Phys. Rev. B: Condens. Matter Mater. Phys.*, 2005, **71**, 235415.
99 A. P. Bartók, R. Kondor and G. Csányi, *Phys. Rev. B: Condens. Matter Mater. Phys.*, 2013, **87**, 184115.
100 J. R. Boes, M. C. Groenenboom, J. A. Keith and J. R. Kitchin, *Int. J. Quantum Chem.*, 2016, **116**, 979–987.
101 A. P. Bartók, J. Kermode, N. Bernstein and G. Csányi, *Phys. Rev. X*, 2018, **8**, 041048.
102 A. Kolmogorov, PhD thesis, The Pennsylvania State University, 2004.
103 J. H. Holland, *Adaptation in natural and artificial systems: an introductory analysis*, University of Michigan Press, Ann Arbor, MI, 1975.
104 D. E. Goldberg, *Genetic algorithms in search, optimization, and machine learning*, Addison-Wesley, Reading, MA, 1989, vol. 27, p. 27.
105 M. Mitchell, *An Introduction to Genetic Algorithms*, MIT Press, Cambridge, MA, 1998.
106 A. N. Kolmogorov, *Module for Ab Initio Structure Evolution*, 2015, http://maise-guide.org.
107 A. N. Kolmogorov, S. Shah, E. R. Margine, A. F. Bialon, T. Hammerschmidt and R. Drautz, *Phys. Rev. Lett.*, 2010, **105**, 217003.
108 A. N. Kolmogorov, S. Shah, E. R. Margine, A. K. Kleppe and A. P. Jephcoat, *Phys. Rev. Lett.*, 2012, **109**, 75501.
109 A. G. Van Der Geest and A. N. Kolmogorov, *CALPHAD: Comput. Coupling Phase Diagrams Thermochem.*, 2014, **46**, 184–204.
110 F. Sun, H. Zheng, Y. Liu, E. D. Sandoval, C. Xu, J. Xu, C. Q. Jin, C. J. Sun, W. G. Yang, H. K. Mao, J. F. Mitchell, A. N. Kolmogorov and D. Haskel, *Phys. Rev. B*, 2018, **98**, 085131.
111 E. D. Sandoval, S. Hajinazar and A. N. Kolmogorov, *Phys. Rev. B*, 2016, **94**, 094105.
112 A. F. Bialon, T. Hammerschmidt, R. Drautz, S. Shah, E. R. Margine and A. N. Kolmogorov, *Appl. Phys. Lett.*, 2011, **98**, 081901.
113 Q. Zhu, V. Sharma, A. R. Oganov and R. Ramprasad, *J. Chem. Phys.*, 2014, **141**, 154102.
114 W.-L. Ng and B. L. Bassler, *Annu. Rev. Genet.*, 2009, **43**, 197–222.
115 M. B. Miller and B. L. Bassler, *Annu. Rev. Microbiol.*, 2001, **55**, 165–199.
116 P. Neuhaus, *Lecture Notes in Computer Science (including subseries Lecture Notes in Artificial Intelligence and Lecture Notes in Bioinformatics)*, Berlin, Heidelberg, 1991, pp. 170–175.
117 S. Habershon, K. D. M. Harris and R. L. Johnston, *J. Comput. Chem.*, 2003, **24**, 1766–1774.
118 G. Trimarchi, A. J. Freeman and A. Zunger, *Phys. Rev. B: Condens. Matter Mater. Phys.*, 2009, **80**, 92101.
119 S. V. Lepeshkin, V. S. Baturin, Y. A. Uspenskii and A. R. Oganov, *J. Phys. Chem. Lett.*, 2019, **10**, 102–106.
120 A. Shayeghi, D. Götz, J. B. Davis, R. Schäfer and R. L. Johnston, *Phys. Chem. Chem. Phys.*, 2015, **17**, 2104–2112.
121 A. Aguado, A. Vega, A. Lebon and B. von Issendorff, *Angew. Chem., Int. Ed.*, 2015, **54**, 2111–2115.
122 A. Stukowski, *Modell. Simul. Mater. Sci. Eng.*, 2012, **20**, 045021.
123 K. Michaelian, N. Rendón and I. L. Garzón, *Phys. Rev. B: Condens. Matter Mater. Phys.*, 1999, **60**, 2000–2010.
124 L. O. Paz-Borbón, R. L. Johnston, G. Barcaro and A. Fortunelli, *J. Chem. Phys.*, 2008, **128**, 134517.
125 V. G. Grigoryan, D. Alamanova and M. Springborg, *Phys. Rev. B: Condens. Matter Mater. Phys.*, 2006, **73**, 115415.
126 S. F. Li, X. J. Zhao, X. S. Xu, Y. F. Gao and Z. Zhang, *Phys. Rev. Lett.*, 2013, **111**, 115501.
127 X. Yang, W. Cai and X. Shao, *J. Phys. Chem. A*, 2007, **111**, 5048–5056.
128 D. Schebarchov, F. Baletto and D. J. Wales, *Nanoscale*, 2018, **10**, 2004–2016.
129 M. Eckhoff, D. Schebarchov and D. J. Wales, *J. Phys. Chem. Lett.*, 2017, **8**, 5402–5407.
130 R. Ferrando, A. Fortunelli and G. Rossi, *Phys. Rev. B: Condens. Matter Mater. Phys.*, 2005, **72**, 085449.
131 A. N. Kolmogorov, S. Hajinazar, C. Angyal, V. L. Kuznetsov and A. P. Jephcoat, *Phys. Rev. B: Condens. Matter Mater. Phys.*, 2015, **92**, 144110.
132 J. Shao, C. Beaufils and A. N. Kolmogorov, *Sci. Rep.*, 2016, **6**, 28369.
133 M. R. Filip, X. Liu, A. Miglio, G. Hautier and F. Giustino, *J. Phys. Chem. C*, 2018, **122**, 158–170.

